

**Near-Infrared Spectroscopy and a Search for CO Emission in  
Three Extremely Luminous *IRAS* Sources; IRAS F09105+4108,  
IRAS F15307+3252, and PG 1634+706**

A. S. Evans<sup>1,2</sup> and D. B. Sanders

Institute for Astronomy, 2680 Woodlawn Drive, Honolulu, HI 96822; ase@astro.caltech.edu,  
sanders@galileo.ifa.hawaii.edu

R. M. Cutri

IPAC, MS 100-22, California Institute of Technology, Pasadena, CA 91125;  
roc@ipac.caltech.edu

S. J. E. Radford

National Radio Astronomy Observatory<sup>3</sup>, Tucson, AZ 85721; sradford@nrao.edu

J. A. Surace

Institute for Astronomy, 2680 Woodlawn Drive, Honolulu, HI 96822;  
jason@galileo.ifa.hawaii.edu

P. M. Solomon

---

<sup>1</sup>Present Address: Dept. of Astronomy 105-24, California Institute of Technology, Pasadena, CA 91125

<sup>2</sup>Guest Observer at the James Clerk Maxwell Telescope, which is operated by the Royal Observatory Edinburgh on behalf of the United Kingdom Science and Engineering Research Council (SERC), the Netherlands Organization for the Advancement of Pure Research (ZWO), and the Canadian National Research Council (NRC).

<sup>3</sup> The NRAO is a facility of the National Science Foundation operated under cooperative agreement by Associated Universities, Inc.

Astronomy Program, State University of New York, Stony Brook, NY 11794;  
psolomon@sbast7.ess.sunysb.edu

D. Downes

Institut de Radio Astronomie Millimétrique, 38406 St. Martin d'Hères, France;  
downes@iram.fr

C. Kramer

Physikalishes Institut, Universitaet zu Koeln, Zuelpicher Strasses 77, D-50937 Koeln,  
Germany; kramer@ph1.uni-koeln.de

Received \_\_\_\_\_; accepted \_\_\_\_\_

## ABSTRACT

Rest-frame 0.48–1.1  $\mu\text{m}$  emission line strengths and molecular gas mass ( $\text{H}_2$ ) upper limits for three luminous infrared sources – the hyperluminous infrared galaxies<sup>4</sup> IRAS F09105+4108<sup>5</sup> ( $z = 0.4417$ ), IRAS F15307+3252 ( $z = 0.926$ ), and the optically-selected QSO PG 1634+706 ( $z = 1.338$ ) – are presented. Diagnostic emission-line ratios ( $[\text{O III}] \lambda 5007/\text{H}\beta$ ,  $[\text{S II}] \lambda\lambda 6716, 6731/\text{H}\alpha$ ,  $[\text{N II}] \lambda 6583/\text{H}\alpha$ , and  $[\text{S III}] \lambda\lambda 9069+9532/\text{H}\alpha$ ) indicate a Seyfert 2-like spectrum for both infrared galaxies, consistent with previously published work. The upper limits of molecular gas mass for all three sources are  $M(\text{H}_2) < 1 - 3 \times 10^{10} h^{-2} M_\odot$  ( $q_0 = 0.5$ ,  $H_0 = 100h \text{ km s}^{-1} \text{ Mpc}^{-1}$ ), less than that of the most gas-rich infrared galaxies in the local Universe. All three sources have  $L_{\text{ir}}/L'_{\text{CO}} \sim 1300 - 2000$ , and thus are the extragalactic sources with the most extreme  $L_{\text{ir}}/L'_{\text{CO}}$  values measured to date. Given the relatively warm far-infrared colors for all three objects, much of their infrared luminosity may emanate from a relatively modest amount of warm dust (e.g.  $M_{\text{d}} \sim 10^{5-7} M_\odot$ ,  $T_{\text{d}} = 200 - 100 \text{ K}$ ) near the AGN. For F09105+4108 and F15307+3252, the implied circumnuclear covering factor of this dust is  $\sim 90\%$ , while for PG 1634+706 the covering factor is only  $\sim 35\%$ .

---

<sup>4</sup>HyLIGs:  $L_{\text{ir}} \geq 10^{13} L_\odot$  where  $L_{\text{ir}} \equiv L(8 - 1000 \mu\text{m})$  and assuming  $H_0 = 75 \text{ km s}^{-1} \text{ Mpc}^{-1}$  and  $q_0 = 0$  (e.g. Sanders & Mirabel 1996). Additional infrared galaxy definitions used throughout this paper – Luminous Infrared Galaxies (LIGs): galaxies with  $L_{\text{ir}} = 10^{11-11.99} L_\odot$ , Ultraluminous Infrared Galaxies (ULIGs): galaxies with  $L_{\text{ir}} \geq 10^{12} L_\odot$ . Throughout this paper, we adopt  $H_0 = 100h \text{ km s}^{-1} \text{ Mpc}^{-1}$  and  $q_0 = 0.5$ .

<sup>5</sup>The source prefix ‘F’ will be used throughout this paper as a shorthand to refer to sources listed in the IRAS Faint Source Catalog (FSC: Moshir et al. 1992).

*Subject headings:* galaxies: ISM—infrared: galaxies—ISM: molecules—radio  
lines: galaxies—galaxies: active

## 1. Introduction

Studies of ultraluminous infrared galaxies (ULIGs) detected by *IRAS* have focussed on revealing the nature of the host galaxies and the source powering the enormous infrared luminosities. Three forms of spectroscopic evidence for both stellar and nonstellar energy sources exists: (1) Studies of ULIGs comparing the fluxes of hydrogen recombination lines with optical and near-infrared forbidden lines have shown that the dominant ionization process appears to differ from galaxy to galaxy. Emission-line diagnostics have been used to classify these galaxies as H II region-like galaxies (i.e., emission lines induced by hot OB stars), Low Ionization Nuclear Emission-line Regions galaxies (LINERs), or Seyferts (e.g., Sanders et al. 1988b; Kim et al. 1995; Kim 1995; Veilleux et al. 1995). (2) Spectral polarimetry of ULIGs often reveal highly polarized continuum and broad emission-line spectrum, indicating the presence of a buried AGN (e.g., Kay & Miller 1989; Hines 1991; Hines 1994; Hines & Wills 1993; Jannuzi et al. 1994). (3) Millimeter-wave (CO) spectroscopy of ULIGs has shown them to be rich in molecular gas, indicating the presence of an enormous amount of material for fueling an active galactic nucleus (AGN) and star formation (e.g., Young et al. 1984; Sanders and Mirabel 1985; Sanders et al. 1987; Scoville et al. 1986; Sanders, Scoville, Soifer 1991; Sanders 1991). In addition, morphological studies of ULIGs have revealed that they commonly have tidal distortions and nearby companions indicative of the merger of two or more galaxies (e.g. Sanders et al. 1988a,b). Sanders et al. 1988a,b have suggested that ULIGs may be the precursor to optically-selected quasars.

The recent discovery of the high-redshift HyLIG IRAS 10214+4724 ( $z = 2.286$ : Rowan-Robinson et al. 1991) and the subsequent detection of molecular gas in the source (Brown & Vanden Bout 1991, 1992; Solomon, Downes, & Radford 1992a), as well as evidence that it harbors a buried AGN (e.g. Elston et al. 1994; Jannuzi et al. 1994), has sparked interest in searching for and studying more luminous IRAS galaxies at early

epochs of the universe. To date, there are two other published findings of  $z > 0.3$  galaxies discovered by *IRAS* – F09105+4108 ( $z = 0.4417$ : Kleinmann & Keel 1987; Kleinmann et al. 1988) and F15307+3252 ( $z = 0.926$ : Cutri et al. 1994), and surveys are underway to search for additional candidates. In addition, a significant fraction of moderate-to-high redshift QSOs were detected by *IRAS*, making observations that test the infrared galaxy-QSO evolutionary hypothesis at higher redshift (and higher luminosities) feasible. To date, 2 local QSOs (Mrk 1014: Sanders, Scoville, & Soifer 1988a; IZw 1: Barvainis, Alloin, & Antonucci 1989), one moderate-redshift quasar (3C 48 at  $z = 0.3695$ : Scoville et al. 1993; Wink et al. 1997), and 2 higher redshift QSOs (the gravitationally lensed H 1413+117 at  $z = 2.556$ : Barvainis et al. 1994; BR 1202-07 at  $z = 4.695$ : Ohta et al. 1996; Omont et al. 1996) have been unambiguously detected in CO.

In this paper, we present CO observations and near-infrared spectroscopy of the high redshift HyLIGs F09105+4108, F15307+3252, and PG 1634+706 (IRAS 16347+7037: e.g. Sanders et al. 1989), the latter of which is the most infrared luminous, optically-selected QSO detected by *IRAS* in the PG sample. The purpose of these observations is to extend the determination of molecular gas properties and dominant ionization mechanisms to distant sources with extreme  $L_{\text{ir}}$ , as well as to establish whether their properties are consistent with the trends in such properties observed for local ULIGs and QSOs.

This paper is divided into 5 sections. The near-infrared and millimeter observing procedures are discussed in §2. The data reduction methods and line-flux calculations are summarized in §3. Section 4 begins with a brief discussion of the optical and infrared morphologies of the three sources, then the dominant ionization mechanism in the two IRAS galaxies, the interpretation of the  $L_{\text{ir}}$  and  $L'_{\text{CO}}$  of the 3 sources, and their spectral energy distributions are examined. Section 5 summarizes the results. Throughout this paper, we adopt  $H_0 = 100h \text{ km s}^{-1} \text{ Mpc}^{-1}$  and  $q_0 = 0.5$ .

## 2. Observations

Tables 1–4 summarize basic information and a journal of observations for the 3 sources discussed in this paper. Observations with each of the telescopes used are discussed separately below. A more in depth discussion of the observing technique and the difficulties inherent in millimeter-wave and submillimeter-wave observations of faint sources can be found in Evans et al. (1996).

### 2.1. Imaging

All of the imaging data were obtained at the UH 2.2m Telescope on Mauna Kea. The near-infrared imaging data were taken with the UH QUick Infrared Camera (QUIRC: Hodapp et al. 1996), which consists of a 1024x1024 pixel HgCdTe Astronomical Wide Area Infrared Imaging (HAWAII) array. The R-band image of F15307+3252 and the I-band image of PG 1634+706 were taken with the UH Tektronix 2048x2048 CCD camera (Wainscoat 1996). Finally, the I-band image PG 1634+706 was obtained with the Orbit Semiconductor 2048x2048 CCD camera (Wainscoat 1996), reimaged to f/10. With the exception of the R-band image of F15307+3252 which consisted of one long exposure, all observations were done by taken a series of dithered exposures.

### 2.2. Near-Infrared Spectroscopy

#### 2.2.1. UH 2.2m Telescope

All spectroscopic observations on the UH 2.2m telescope were made with the K-band spectrograph (KSPEC: Hodapp et al. 1994). KSPEC is a cross-dispersed echelle configured to cover the wavelength range 1.1–2.5  $\mu\text{m}$  in 3 orders (*J*, *H*, and *K*) on a 256×256



NICMOS-3 HgCdTe detector array. The wavelength resolutions (at  $2.2 \mu\text{m}$ ) for each of the observations are listed in Table 3. Additionally, the wavelength range  $0.7\text{--}1.0 \mu\text{m}$  is also dispersed in several orders on the array. However, the order crowding at  $0.7\text{--}1.0 \mu\text{m}$  is such that only spectra of point-like sources can effectively be extracted, and this wavelength range is also compromised due to the fact that KSPEC is only in focus at  $\lambda > 0.85 \mu\text{m}$ . In addition to its spectral capabilities, KSPEC also provides simultaneous imaging of approximately one square arcminute of sky around the slit on a second NICMOS-3 array. For the 1994 December observing period, the new UH tip-tilt system (Jim et al. 1997) was also implemented, notably improving the tracking, offsetting, and seeing of the observations and data.

Each observing night began with a series of flat field exposures in the closed dome with incandescent lights turned on, then off. Once the telescope was guiding with the source in the slit, a 180-second exposure was taken, followed by a 180-second exposure 10 arcseconds off-source. Each spectrum exposure was accompanied by a 140-second image exposure. For the March observations, the pattern for observing was source-sky-source-sky, etc., but the pattern was changed to source-sky-sky-source-source-sky-sky-source, etc. for the December observations to minimize spurious features created by the changing sky conditions. Observations of standard A (V) stars near each source were also made to flux calibrate the source spectrum and to remove telluric lines, and observations of an argon lamp were made to wavelength calibrate the KSPEC data.

### *2.2.2. United Kingdom Infrared Telescope (UKIRT)*

Observations of F15307+3252 were made with the upgraded Cooled Grating Spectrometer (CGS4) on the 3.8m UKIRT in shared-risk time. CGS4 is a  $1\text{--}5 \mu\text{m}$  2D grating spectrometer with a  $256 \times 256$  InSb array. Because the  $\text{H}\alpha + [\text{N II}] \lambda 6583$  and  $[\text{S}$

II]  $\lambda\lambda 6716,6731$  (hereafter [S II]  $\lambda 6724$ ) emission from the source is redshifted to J-band, the 75 line  $\text{mm}^{-1}$  grating in second order was used. Sampling was done by moving the detector over 2 pixels in 6 steps in the wavelength direction. For the observations, a 1 pixel-wide (1.2 arcsecond) slit was used.

Spectral data was taken in 120-second exposures, with 20 seconds of each exposure made at each detector position during the 2-pixel sampling. The slit was then moved 15 arcseconds in the spatial axis direction of the array for the next 120 second exposure. Thus, the source appears on the array as a positive and negative spectrum after the first frame is subtracted from the second. The source-sky observation sequence was the same as that used in the 1994 December KSPEC observations. Observations of the standard A star HD 162208 were made before and after the observations of F15307+3252. A krypton lamp was used as the wavelength calibration source.

We encountered a problem with CGS4; the source flux of the positive spectrum was more than of the negative spectrum flux, implying that the source was only partially in the slit in the second position. Alternatively, the flux of the positive A star spectrum was less than the negative spectrum flux. The slit also appeared to be tilted relative to the array as evident by the position of the OH sky lines. Because of this, only half the data had enough flux to be usable, and no photometry was possible.

## 2.3. Submillimeter Spectroscopy

### 2.3.1. James Clerk Maxwell Telescope (JCMT)

Observations with the 15m JCMT Telescope were made using the 1mm spectral line receiver (A2), together with the Digital Autocorrelation Spectrometer (DAS) in wide-band mode (750 MHz bandwidth). Because of excess noise near the edge of the passband, the

usable bandwidth was only  $\sim 700$  MHz, which corresponds to a total velocity coverage of  $\sim 900$  km s $^{-1}$  at 230 GHz.

All observations were obtained using a nutating subreflector with a chop rate of  $\sim 1.25$  Hz. Data were stored as six minute scans, and a chopper wheel calibration was performed after every other scan. Pointing was monitored every few hours by observations of standard continuum sources and was estimated to be accurate to within a few arcseconds. During the course of the observations, data were also taken with the bandpass centered at velocity offsets  $\pm 40$  km s $^{-1}$  from the velocity corresponding to the redshift of the optical emission lines. Shifting the velocities in such a manner minimizes any ripples inherent in the baseline.

### *2.3.2. Instituto de Radio Astronomía Milimétrica (IRAM) 30m Telescope*

The IRAM telescope has the ability to perform observations using the 3mm, 2mm, and 1mm receivers simultaneously, making use of the 2 available 512 MHz filterbanks and two 512 MHz autocorrelators. For F09105+4108, the 2mm and 1mm receivers were tuned to the redshifted CO(2  $\rightarrow$  1) and CO(3  $\rightarrow$  2) transitions, respectively. During the observations, pointing was monitored by observing the planets and standard continuum sources and was typically accurate to within 3 arcseconds.

### *2.3.3. National Radio Astronomy Observatory (NRAO) 12m Telescope*

Observations of the redshifted CO(2  $\rightarrow$  1) emission in PG 1634+706 were made with the NRAO 12m Telescope configured with a dual polarization SIS spectral-line receiver and two  $256 \times 2$  MHz channel filterbanks. Observations were obtained using a nutating subreflector with a chop rate of  $\sim 1.25$  Hz. Six minute scans were taken, and a calibration was done every other scan. The pointing was checked every few hours by observing Jupiter

and was estimated to be accurate to within a few arcseconds. Because the duration of the observation was equivalent to one source transit, no velocity shifts were made.

### 3. Results

#### 3.1. Imaging Data

The I-band data reduction was done with IRAF. The data reduction consisted of flatfielding the individual images, scaling each image to its median value, and shifting and averaging the images.

The  $K'$ -band data reduction was done similar to the I-band data reduction, except that after the median level of each individual frame was subtracted, the individual frames were averaged together (without spatial shifting) using a minmax averaging routine in order to create a “sky” image. This sky image was subtracted from the individual frames before they were shifted and averaged.

Because the R-band image of F15307+3252 consisted of one integration, the image was simply flatfielded and scaled to its median value. Cosmic rays were then removed from the area around the galaxy. With the exception of the  $K'$ -band image of PG 1634+706, which shows only the unresolved point-like QSO, the final reduced versions of all the images are shown in Figures 1–3.

#### 3.2. Near-Infrared Spectra

The KSPEC data reduction was done with IRAF. The sky frames were first subtracted from the source frames. The sky subtracted frames were then averaged and divided by the flat fields. Because there were only a few bad pixels and none were on the spectral area

containing the source spectrum, the bad pixels were individually set to zero before the spectral orders were extracted with the APALL package. The extracted spectra were then wavelength calibrated and divided by the standard star spectrum, reduced in the same fashion as the source spectrum, to remove any instrumental effects and atmospheric lines (note that the stellar absorption lines in the standard star were removed using the IRAF task SPLOT before the division was done). Because of the narrow width of the slit, no photometry was determined for any of the KSPEC observations. Finally the spectrum was multiplied by a Planck blackbody spectrum with the same temperature as the standard star.

Table 5 summarizes the emission-line properties determined for F09105+4108 and F15307+3252. The emission-line fluxes,  $f(\lambda)$ , line widths,  $\Delta v_{\text{FWHM}}$ , and root-mean-square flux densities,  $S_{\text{rms}}$ , were determined using the IRAF task SPLOT. The signal-to-noise ratios were determined by using the expression  $f(\lambda)/\Delta v_{\text{FWHM}}S_{\text{rms}}$ .

The CGS4 data were reduced in a same manner as the KSPEC data, except that the flat fielding and masking of bad pixels was done automatically after every observation.

Figure 4 shows the spectra of F09105+4108 obtained with KSPEC. Six of the eight emission lines detected are at wavelengths corresponding to a source redshift of  $z = 0.4417$ , identical to the observer-frame optical redshift determined by Kleinmann et al. (1988). The discrepancy in the [O III]  $\lambda\lambda 4959, 5007$  doublet redshift ( $z = 0.4429$ ) is due to wavelength calibration inaccuracies (the overlapping of the last few orders made it difficult to determine which argon line was in which order).

Figure 5 shows the spectra of F15307+3252 obtained with KSPEC and the J-band spectrum obtained with CGS4. The KSPEC spectral lines imply a source redshift of  $z = 0.926$ , and the CGS4 spectra imply a redshift of  $z = 0.927$ , both consistent with the redshift of 0.926 determined by Cutri et al. (1994). Note that both F09105+4108 and

F15307+3252 show strong forbidden-line emission. Further, the  $H\alpha$ + $[N\ II]\ \lambda\lambda 6548 + 6583$  and  $[S\ II]\ \lambda 6724$  lines widths of F09105+4108 (Table 5) are consistent with those measured from median resolution spectroscopy by Liu, Graham, & Wright (1996). The interpretation of the line emission will be discussed in §4.2.

To determine the fluxes of the  $H\alpha$  and  $[N\ II]\ \lambda\lambda 6548+6583$  lines of F09105+4108 and F15307+3252, the line profiles were fit using the IRAF package SPECFIT. Initial guesses to the fluxes and line widths were entered into the program, and the line flux ratios and wavelength ratio of  $[N\ II]\ \lambda 6583$  to  $[N\ II]\ \lambda 6548$  were fixed to 3 and 1.005345 (i.e., the ratio 6583/6548), respectively. In addition, the line widths of the two  $[N\ II]$  lines were fixed to be equal. Iterations were made until a convincing fit was achieved. The best fit models are listed in Table 5.

Figure 6 is a short exposure of the redshifted  $[O\ III]\ \lambda\lambda 4959,5007$  and  $H\alpha$  lines of PG 1634+706. The redshifts determined from the  $\Delta v_{FWHM} = 4600\ \text{km s}^{-1}$   $H\alpha$  line and the  $[O\ III]\ \lambda 5007$  lines are  $z = 1.339$  and  $1.337$ , respectively. The systemic redshift determined by Tytler & Fan (1992) is 1.3371.

### 3.3. CO Spectra

Table 6 summarizes the CO line data for the 3 sources. In the case of the IRAM 30m observations, where data was taken at several widely spaced velocity offsets, the data are presented in separate spectral blocks. Separating the data in this manner avoids the creation of direct current (dc) offset-induced ghost features (see Evans et al. 1996) and provides data blocks with relatively constant signal-to-noise across each spectrum.

Figures 7–9 show the spectra of F09105+4108, F15307+3252, and PG 1634+706, respectively. For each source, individual scans were examined to check for sinusoids in

the baselines and other irregularities. After bad scans were removed, the rest of the scans were averaged and linear baselines were subtracted. For the JCMT 15m data, where the sources were observed with several small velocity offsets, only the overlapping regions of the scans were averaged. Finally, the spectra were smoothed to 30-50 km s<sup>-1</sup>. No emission lines were detected. More sensitive upper limits of the CO emission in PG 1634+706 and F15307+3252 have also been recently reported by Barvainis et al. (1998) and Yun, Scoville, & Evans (1998), respectively (see Table 6).

### 3.3.1. CO Luminosity and H<sub>2</sub> Mass Limits

Table 6 lists the root-mean-square temperatures,  $T_{\text{rms}}$ , achieved with a velocity resolution,  $\Delta v_{\text{res}}$ , for the 3 sources observed. To calculate the upper limit of the CO line intensity,  $I_{\text{CO}}$ , we assume that the CO lines have a FWHM velocity,  $\Delta v_{\text{FWHM}} \sim 250 \text{ km s}^{-1}$ , similar to CO lines seen in local ULIGs (e.g. Sanders et al. 1991) and in IRAS 10214+4724 (e.g. Solomon et al. 1992a), Using the observed  $T_{\text{rms}}$  and  $\Delta v_{\text{res}}$  from Table 6, the  $3\sigma$  limit on  $I_{\text{CO}}$  is given by

$$I_{\text{CO}} < \frac{3T_{\text{rms}}\Delta v_{\text{FWHM}}}{\sqrt{\Delta v_{\text{FWHM}}/\Delta v_{\text{res}}}} \text{ [K km s}^{-1}\text{]}. \quad (1)$$

Multiplying  $I_{\text{CO}}$  by the Kelvin-to-Jansky conversion for a point source<sup>6</sup> gives the corresponding limit for  $S_{\text{CO}}\Delta v$  [Jy km s<sup>-1</sup>].

The luminosity distance for a source at a given redshift,  $z$ , is,

$$D_L = cH_0^{-1}q_0^{-2} \left\{ zq_0 + (q_0 - 1) \left( \sqrt{2q_0z + 1} - 1 \right) \right\} \text{ [} h^{-1} \text{ Mpc]}, \quad (2)$$

---

<sup>6</sup> Kelvin-to-Jansky conversion factors: JCMT 15m – 15.6 Jy K<sup>-1</sup> (Matthews 1992), IRAM 30m – 4.6 to 4.9 Jy K<sup>-1</sup> (Guelin, Kramer, & Wild 1995), NRAO 12m – 25.2 Jy K<sup>-1</sup> (P. Jewell, private communication)

where  $q_0$  is the deceleration parameter ( $= 0.5$  for a critical density universe) and  $H_0 = 100h$  ( $\text{km s}^{-1} \text{Mpc}^{-1}$ ). Given the estimated upper limit of  $S_{\text{CO}}\Delta v$ , we can calculate the CO luminosity of a source at redshift  $z$ ,

$$L'_{\text{CO}} = \left( \frac{c^2}{2k\nu_{\text{obs}}^2} \right) S_{\text{CO}}\Delta v D_{\text{L}}^2 (1+z)^{-3}, \quad (3)$$

where  $c$  is the speed of light,  $k$  is the Boltzmann constant, and  $\nu_{\text{obs}}$  is the observed frequency. In terms of useful units,  $L'_{\text{CO}}$  for the  $\text{CO}(J \rightarrow J-1)$  rotational transition can be written as,

$$L'_{\text{CO}} = 2.4 \times 10^3 \left( \frac{S_{\text{CO}}\Delta v}{\text{Jy km s}^{-1}} \right) \left( \frac{D_{\text{L}}^2}{\text{Mpc}^2} \right) J^{-2} (1+z)^{-1} [h^{-2} \text{K km s}^{-1} \text{pc}^2]. \quad (4)$$

Table 6 lists the  $L'_{\text{CO}}$  upper limits of the 3 sources observed. We have assumed that CO rotational transitions up to  $\text{CO}(4 \rightarrow 3)$  have approximately the same brightness temperature. This assumption is based on previously published multi-transition CO analyses of the HyLIG IRAS 10214+4724 (e.g. Solomon et al. 1992a). For PG 1634+706, we have assumed that the  $\text{CO}(5 \rightarrow 4)$  transition has approximately the same brightness temperature as the lower transitions, as observed in the Cloverleaf Quasar (Barvainis 1996).

The upper limits on  $\text{H}_2$  masses implied by the observed limits on  $L'_{\text{CO}}$  can be determined by making the reasonable assumption that the CO emission is optically thick and thermalized, and that it originates in gravitationally bound molecular clouds. For molecular gas in gravitationally bound clouds, the ratio of the  $\text{H}_2$  mass and the CO luminosity is given by  $\alpha = M(\text{H}_2)/L'_{\text{CO}} \propto \sqrt{n(\text{H}_2)}/T_{\text{b}} M_{\odot} (\text{K km s}^{-1} \text{pc}^2)^{-1}$ , where  $n(\text{H}_2)$  and  $T_{\text{b}}$  are the density and brightness temperature for the appropriate CO transition (e.g. Sanders & Scoville 1987; Solomon et al. 1992a). Multi-transition CO surveys of molecular clouds in the Milky Way (e.g. Sanders et al. 1993), and in nearby starburst galaxies (e.g. Güsten et al. 1993) have shown that hotter clouds tend to be denser such that the density and temperature dependencies tend to cancel each other. The variation in the value of  $\alpha$  is less than a factor of 2 for a wide range of gas kinetic temperature, gas densities, and



CO abundances. We adopt a value of  $4 M_{\odot} (\text{K km s}^{-1} \text{ pc}^2)^{-1}$  for  $\alpha$ , which is similar to the value determined for the bulk of the molecular gas in the disk of the Milky Way (c.f. Scoville & Sanders 1987), as well as the value determined from a multi-transition CO analysis of IRAS 10214+4724 (Solomon et al. 1992a). Table 6 lists the upper limits on the the molecular gas mass of F09105+4108, F15307+3252, and PG 1634+706 determined using this value of  $\alpha$ .

## 4. Discussion

As stated in the introduction, spectroscopy has been a powerful tool for determining the dominant ionization source in infrared-luminous galaxies. The environment and morphology of the host galaxy are an essential supplement to the spectroscopy, often providing information on global spatial scales that have direct bearing on the nuclear activity. We briefly discuss the imaging data, then dedicate the bulk of the remaining discussion to the spectroscopic data.

### 4.1. Morphologies and Environment

Figures 1-3 show images of the three sources taken at wavelengths longward of V-band. Most local ( $z < 0.3$ ) ultraluminous infrared galaxies are observed to have distorted morphologies, multiple nuclei, and close companions indicative of the merger of two or more galaxies (e.g. Sanders & Mirabel 1996 and references therein; Surace et al. 1997). F09105+4108 clearly shows evidence for companions (Figure 1). Indeed, unlike most luminous infrared galaxies (LIGs), F09105+4108 is clearly a cD galaxy. Both the I and K'-band images of the galaxy show evidence of “clumps” within the envelope of the cD galaxy, which may be galaxies stripped by tidal or dynamical friction. Such stripping may

be the source of dust for F09105+4108. In addition, F09105+4108 is known to have radio jets (Hines & Wills 1993), indicating the presence of a buried AGN.

While the R-band image of F15307+3252 (Figure 2a) shows no direct evidence of distorted morphologies or close companions, the K'-band image (Figure 2b) shows a faint companion to the southwest of the main galaxy. Soifer et al. (1996) and Liu, Graham, & Wright (1996) also present near-infrared images showing this companion, with the latter group showing evidence for a second companion. No evidence is seen for tidal features in Figure 2, or in any other images published to date.

The QSO PG 1634+706 (Figure 3), the most distant of the three sources, shows no evidence of distortions or close companions. There appear to be approximately 30 faint objects in the vicinity of the QSO with  $m_I = 23.5 - 25.5$ , which is consistent with the density of faint field objects expected within the given magnitude range (Pozzetti et al. 1998). Thus, there is also no apparent evidence with the present data set that the QSO is imbedded in a cluster.

## 4.2. Emission-Line Diagnostics

Figure 10 shows 4 emission-line diagnostic diagrams commonly used to distinguish galaxies with Seyfert/LINER-like properties from galaxies with H II region-like properties. The usefulness of these diagrams can be understood by the following emission-line characteristics: Emission from [S II]  $\lambda 6724$  and [N II]  $\lambda\lambda 6548+6583$  can emanate from ionized hydrogen regions, and [S II]  $\lambda 6724$  and [O I]  $\lambda 6300$  emission can emanate from semi-ionized regions where collisional ionization is significant. Enhancement of these lines occurs in AGNs because, unlike H II regions, they have extended partially ionized zones created by an excess of X-rays (the absorption cross sections of neutral hydrogen, helium

and all ions are small for X-rays, thus X-rays tend to escape the ionized region before interacting: Veilleux & Osterbrock 1987). [O III]  $\lambda 5007$  is a high ionization line photoionized by UV photons, and thus tends to be strong in Seyfert galaxies. [S III]  $\lambda\lambda 9069+9532$  is not as sensitive to the level of ionization as [O III]  $\lambda 5007$ , most likely due to its lower ionization potential (Osterbrock, Tran, & Veilleux 1992). However, [S III]  $\lambda\lambda 9069+9532$  and [S II]  $\lambda 6724$  together do provide some degree of separation between the 3 classes of active galaxies (Figure 10d).

Emission-line ratios of F09105+4108 and F15307+3252 are plotted in the diagnostic diagrams. For F09105+4108, the [O III]  $\lambda 5007 / H\beta$  and [O I]  $\lambda 6300 / H\alpha$  ratios have been determined from Kleinmann et al. (1988). Because their [O III]  $\lambda 5007 / H\beta$  ratio is being used in combination with our KSPEC measurements, it is worth cautioning that [O III]  $\lambda 5007 / H\beta$  may vary as a function of the aperture size used to observe F09105+4108. In all 4 diagrams, both galaxies lie in the Seyfert region, indicating that the dominant source of ionization is a hard, nonthermal continuum source. The analysis of these data are consistent with the detection of broad emission lines in polarized light in all three sources (Hines & Wills 1993; Hines et al. 1995; Jannuzi et al. 1994) and previous optical emission-line diagnostics of both galaxies done with low resolution (Soifer et al. 1994, 1996) and median resolution (Kleinmann et al. 1988; Liu, Graham, & Wright 1996) spectroscopy.

Table 7 is a comparison of the observed [O III]  $\lambda 5007 / H\alpha$ , [S II]  $\lambda 6724 / H\alpha$ , and [N II]  $\lambda 6548+6583 / H\alpha$  ratios of F09105+4108 and F15307+3252 with the sample of Bright *IRAS* galaxies and warm *IRAS* galaxies (which have been divided into Seyfert 2, LINER, and H II region classifications). For F09105+4108, the ratio [O III]  $\lambda 5007 / H\alpha$  has been determined from Kleinmann et al. (1988), who calculate [O III]  $\lambda 5007 / H\beta \sim 12$  and a negligible extinction (note that the [O III]  $\lambda 5007 / H\alpha$  ratio calculated from our data indicate that half of the [O III]  $\lambda 5007$  flux is lost via defocussing; see §2.2.1). Despite the

obvious scatter in the [O III]  $\lambda 5007$  /  $H\alpha$  ratio due to dust, there is a notable separation between the ratio for Seyferts and for LINERs and H II region galaxies (i.e., the separation is due mainly to the ionization parameter). While F09105+4108 has a [O III]  $\lambda 5007$  /  $H\alpha$  ratio 2 standard deviations above the average ratio for low-redshift Seyfert 2 galaxies, F15307+3252 have observed [O III]  $\lambda 5007$  /  $H\alpha$  ratio higher than the average Seyfert 2 ratio, but still within the standard deviation of the Seyfert 2 ratios. Inversely, the [S II]  $\lambda 6724$  /  $H\alpha$  and [N II]  $\lambda 6548+6583$  /  $H\alpha$  ratios are lower than the average values of the Seyferts, but still within the standard deviation of the Seyfert 2 ratios. This may imply that the hyperluminous galaxies have smaller semi-ionized regions or lower metallicities than the average, local *IRAS* Seyferts.

### 4.3. $L_{\text{ir}}$ versus $L'_{\text{CO}}$

Given the evidence presented here and elsewhere for AGNs in both F09105+4108 and F15307+3252, we consider the infrared and CO luminosities of these 2 sources and PG 1634+706 relative to LIGs, ULIGs and QSOs detected by *IRAS*, but having lower infrared luminosities. Figure 11a is a plot of  $L'_{\text{CO}}$  vs.  $L_{\text{ir}}$ ; the upper limits on the  $L'_{\text{CO}}$  of F09105+4108, F15307+3252, and PG 1634+706 are less than the  $L'_{\text{CO}}$  of the most gas-rich galaxies observed locally, perhaps indicating that the upward trend of data points in the diagram levels off at higher  $L_{\text{ir}}$ , or disperses. Figure 11b is a plot of  $L_{\text{ir}}/L'_{\text{CO}}$  vs.  $L_{\text{ir}}$ ; the lower limits on the  $L_{\text{ir}}/L'_{\text{CO}}$  of the 3 sources are consistent with the increasing values of  $L_{\text{ir}}/L'_{\text{CO}}$  as a function of increasing  $L_{\text{ir}}$  of the sample of LIGs and ULIGs. One possible explanation for the data trends observed in Figure 11 is that  $L_{\text{ir}}$  becomes increasingly dominated by reprocessed nonstellar light at high  $L_{\text{ir}}$ . From the spectral energy distributions plotted in Figure 12, it is clear that all 3 sources have  $\nu L_{\nu}(60\mu\text{m})/\nu L_{\nu}(100\mu\text{m})$  ratios higher than nearby, less luminous ULIGs that have been detected in CO such as Arp 220 and

Mrk 1014 (e.g. Sanders et al. 1988b). The mass of “warm” dust required to produce the observed infrared luminosity can be computed by fitting the rest-frame far-infrared (40-100  $\mu\text{m}$ ) emission with a single-temperature dust model using dust emissivities from Draine & Lee (1984). The dust temperatures implied by the far-infrared SEDs in Figure 12 are in the range 100–200 K, and the corresponding dust masses,  $M_d = (L_{\text{ir}}/10^8 L_{\odot})(40 \text{ K}/T_d)^5$ , are in the range  $10^7 - 10^5 M_{\odot}$ . Assuming, as is found for ULIGs like Arp 220 and Mrk 1014, that the bulk of the dust is heated to the computed “warm” dust temperature, and that the gas/dust ratio is similar to what is found for other ULIGs such as Arp 220 (i.e.  $\sim 200$ : Sanders, Scoville, & Soifer 1991), then the implied range of  $\text{H}_2$  gas mass is  $10^{9.3} - 10^{7.3} M_{\odot}$ . Thus it is possible that the observed infrared luminosities are produced by a relatively modest mass of gas and dust (e.g. comparable to or less than the total molecular gas mass of the Milky Way) heated to temperatures 100–200 K, perhaps by the central AGN. Such small amounts of molecular gas would also explain our non detections of all three sources in CO (see Table 6). Further, while it is clear from the observed narrow emission lines and large infrared excess ( $L_{\text{ir}}/L_{\text{bol}} > 0.9$ ) of F09105+4108 and F15307+3252 that the circumnuclear covering factor of the dust is almost unity, the broad emission lines and smaller infrared excess ( $L_{\text{ir}}/L_{\text{bol}} \sim 0.35$ ) of PG 1634+706 indicate that the QSO has a low covering factor.

It is curious that CO surveys of galaxies at cosmological distances have yielded no evidence of galaxies with  $L'_{\text{CO}}$  much larger than that of the most CO luminous galaxies at lower redshift ( $z \lesssim 0.2$ ) plotted in Figure 11 (i.e.,  $L'_{\text{CO}}$  corresponding to  $\sim 3-4 \times 10^{10} h^{-2} M_{\odot}$  of molecular gas). To date, there exists little evidence that the  $\text{H}_2$  content of active galaxies evolves with redshift ( $z \lesssim 4$ ). The extremely high  $\text{H}_2$  masses originally computed for IRAS 10214+4724 and H 1413+117 were in large part due to gravitational lensing of these sources by foreground objects (IRAS 10214+4724: Elston et al. 1994; Soifer et al. 1995; Trentham 1995; Graham & Liu 1995; Broadhurst & Lehar 1995; Serjeant et al. 1995;

Close et al. 1995; Eisenhardt et al. 1995; Downes, Solomon, & Radford 1995; H 1413+117: Barvainis et al. 1994), and CO surveys of  $1 < z < 4$  high redshift powerful radio galaxies (HzPRGs: Evans et al. 1996; Downes et al. 1996) and  $z \sim 4$  luminous high redshift QSOs (Barvainis & Antonucci 1996) were unsuccessful at detecting sources with more molecular gas than the most gas-rich galaxies observed locally (i.e. based on  $3\sigma$  upper  $M(\text{H}_2)$  limits of the HzPRGs and high redshift QSOs). The reported detection of CO emission in the  $z = 4.7$  QSO BR 1202-07 ( $M(\text{H}_2) \sim 6 \times 10^{10} h^{-2} M_\odot$ ) may be the first indication that  $M(\text{H}_2)$  increases beyond  $z \sim 4$ . However, reports of shear due to gravitational lensing in the vicinity of BR 1202-07 may mean that the CO luminosity is being amplified (e.g. see discussion in Omont et al. 1996b). Further, there have been recent, unconfirmed detections of CO emission in the  $z = 2.4$  radio galaxy 53W002 (Scoville et al. 1997), the  $z = 4.5$  QSO BR 1335-07 (Guilloteau et al. 1998), and the gravitationally lensed,  $z = 2.6$  quasar MG 0414+0534 (Barvainis et al. 1998), but all have molecular gas masses comparable to the most gas-rich, local galaxies.<sup>7</sup> The inferred molecular gas masses and upper limits of high redshift galaxies surveyed to date may be evidence that either galaxies with more than  $\sim 3\text{--}4 \times 10^{10} h^{-2} M_\odot$  of molecular gas rapidly turn the gas into stars, and/or that galaxies form in a hierarchical fashion. It may also be the case that only high-redshift galaxies with a significant nonstellar contribution to their infrared luminosity will be observed to have high  $L_{\text{ir}}$ . A better understanding of the relationship between extreme  $L_{\text{ir}}$  and  $\text{H}_2$  mass awaits the detection and observation of a larger sample of HyLIGs, especially those having relatively cool *IRAS* colors, i.e. relatively low values of  $\nu L_\nu(60\mu\text{m})/\nu L_\nu(100\mu\text{m})$ .

---

<sup>7</sup>This statement assumes that the observed CO emission in MG 0414+0534 is gravitationally lensed by at least three times its intrinsic luminosity.

## 5. Summary

We have presented new millimeterwave CO(J+1,J) observations and rest-frame 0.48–1.1  $\mu\text{m}$  spectroscopy of the HyLIGs IRAS F09105+4108, IRAS F15307+3252, and PG 1634+706. The following conclusions are drawn:

(1) The emission line ratios [O III]  $\lambda$ 5007/H $\beta$ , [O I]  $\lambda$ 6300/H $\alpha$ , [N II]  $\lambda$ 6583/H $\alpha$ , [S II]  $\lambda$ 6724/H $\alpha$ , [S III]  $\lambda$  $\lambda$ 9069+9532/H $\alpha$  of F09105+4108 and F15307+3252 indicate that both have Seyfert 2 emission-line spectra, consistent with previously published work.

(2) Our upper limits on the molecular gas mass of the 3 HyLIGs are comparable to or less than the H<sub>2</sub> mass of the most gas-rich galaxies observed locally.

(3) The relatively “warm” far-infrared (60  $\mu\text{m}$ /100  $\mu\text{m}$ ) colors (implying dust temperatures  $T_d = 100 - 200$  K) for all three sources are consistent with the idea that the bulk of their infrared emission emanates from a relatively modest amount of warm circumnuclear dust, i.e.  $M_d = 10^5 - 10^7 M_\odot$ , corresponding to a molecular gas mass,  $M(\text{H}_2) \simeq 10^{7.3} - 10^{9.3} M_\odot$ . This would be consistent with our measured upper limits for  $L'_{\text{CO}}$  and the corresponding extreme values of  $L_{\text{ir}}/L'_{\text{CO}}$ .

(4) While the narrow emission lines and  $L_{\text{ir}}/L_{\text{bol}} > 0.90$  of F09105+4108 and F15307+3252 indicate a circumnuclear dust covering factor of almost unity, the broad emission lines and  $L_{\text{ir}}/L_{\text{bol}} \sim 0.35$  of PG 1634+706 indicate that most of the AGN is exposed.

We thank the staffs of the JCMT 15m telescope, the IRAM 30m telescope, the NRAO 12m telescope, the UH 2.2m telescope, and the United Kingdom Infrared Telescope for their generous support during our observations. A.S.E. thanks N. Trentham, E. Egami, J. Hora, D. Kim, T. Greene, P. Hall, and J. Goldader for useful discussions and assistance during the

preparation of this paper. A.S.E. is also indebted to J. Jensen and D. Jewitt for obtaining part of the  $K'$ -band and the R-band image data, respectively, of F15307+3252, and to J. Mazzeella for help in obtaining the IRAS SCANPI flux measurements for all three sources. We also thank K. Teramura for the final preparation of figures show in this paper, and the referee, Sylvain Veilleux, for many useful comments. A.S.E. was supported in part by NASA grant NAG5-3042. D.B.S. was supported in part by NASA grant NAG5-3370. This research has made use of the NASA/IPAC Extragalactic Database (NED) which is operated by the Jet Propulsion Laboratory.



Table 1. Source Parameters

Name	R.A.	Dec.	$f_\nu(\lambda)$ (Jy)				$z$	Refs	$L_{\text{ir}}^{\text{a}}$ ( $L_\odot$ )
			$12\mu\text{m}$	$25\mu\text{m}$	$60\mu\text{m}$	$100\mu\text{m}$			
F09105+4108 <sup>b</sup>	09:10:32.84	41:08:53.6	0.13±.03	0.33±.03	0.53±.04	<0.32	0.4417	1,3,4	$7.8 \times 10^{12} h^{-2}$
F15307+3252	15:30:44.63	32:52:50.6	<0.07	0.08±.07	0.26±.08	0.46±0.19	0.926	1,3,4	$2.5 \times 10^{13} h^{-2}$
F16348+7037 (PG 1634+706)	16:34:51.0	70:37:37.0	0.06±.01	0.13±.01	0.25±.03	<0.45	1.337	2,3,5	$5.7 \times 10^{13} h^{-2}$

<sup>a</sup>Assuming  $q_o = 0.5$ ,  $H_o = 100h \text{ km s}^{-1} \text{ Mpc}^{-1}$ .

<sup>b</sup>IRAS Point Source Catalog name in Kleinmann et al. (1988) was P09104+4109

References. — Positions, fluxes, and redshifts: (1) Becker et al. (1995); (2) This paper (IRAS FSC); (3) This paper (IRAS SCANPI); (4) This paper (near-infrared emission lines); (5) Titler & Fan (1992)

Table 2. Journal of Imaging Observations

Source	Telescope	Detector	Pixel Scale <sup>a</sup> arcsec/pixel	Band	Date m/y	Time min.
IRAS F09105+4108	UH 2.2m	Tek	0.14	I	03/97	26
		QUIRC	0.19	K'	04/96	30
IRAS F15307+3252	UH 2.2m	Tek	0.22	R	04/94	20
		QUIRC	0.19	K'	04/96	60
PG 1634+706	UH 2.2m	Orbit	0.14	I	06/97	55
		QUIRC	0.06	K'	05/97	16

<sup>a</sup>Imaging at the UH 2.2m Telescope is done with a focal ratio of f/10 or f/31. For the CCD observations, images taken at f/31 are binned 2×2 pixels.

Table 3. Journal of Near-Infrared Spectroscopic Observations

Name	Telescope	Detector	Slit Width	$\frac{\lambda}{\Delta\lambda}$	Date	Time
			"		mm/yy	min
IRAS F09105+4108	UH 2.2m	KSPEC	1.0	620	12/94	18
IRAS F15307+3252	UH 2.2m	KSPEC	0.8	760	03/94	33
	UKIRT	CGS4	1.2	1000	05/95	56
PG 1634+706	UH 2.2m	KSPEC	1.0	760	03/94	3

Table 4. Journal of CO Observations

Name	line	Telescope	Date	Time	$T_{\text{sys}}$
			m/y	hr	K
IRAS F09105+4108	CO(3 $\rightarrow$ 2)	JCMT 15m	04/94	7.3	429
	CO(3 $\rightarrow$ 2)	IRAM 30m	06/94	6.3	724
	CO(2 $\rightarrow$ 1)	IRAM 30m	06/94	6.3	530
IRAS F15307+3252	CO(4 $\rightarrow$ 3)	JCMT 15m	03/94	8.4	380
	CO(4 $\rightarrow$ 3)	JCMT 15m	04/94	1.7	400
	CO(4 $\rightarrow$ 3)	IRAM 30m	06/94	10.2	590
PG 1634+706	CO(5 $\rightarrow$ 4)	JCMT 15m	04/94	11.0	452
	CO(2 $\rightarrow$ 1)	NRAO 12m	05/94	5.6	160

Table 5. Near-Infrared Spectroscopy; Emission Line Properties

		IRAS F09105+4108				IRAS F15307+3252			
Line	Instr.	$\lambda_{\text{obs}}$ (Å)	$f(\lambda)/f([\text{SII}])$	FWHM <sup>a</sup> (km s <sup>-1</sup> )	$S/N$	$\lambda_{\text{obs}}$ (Å)	$f(\lambda)/f([\text{SII}])$	FWHM <sup>a</sup> (km s <sup>-1</sup> )	$S/N$
H $\beta$	KSPEC	...	...	...	...	...	< 1.4	(1300)	...
[O III] $\lambda$ 4959	KSPEC	7153.1	2.6 $\pm$ 0.8	740	3.2	9556.5	5.5 $\pm$ 0.4	1540	12
[O III] $\lambda$ 5007	KSPEC	7224.6	9.0 $\pm$ 1.0	980	8.9	9644.6	16 $\pm$ 0.4	1280	35
[O I] $\lambda$ 6300	KSPEC	...	< 0.44	(1000)	...	...	< 1.0	(1300)	...
H $\alpha$ + [N II]	KSPEC	9463.5 <sup>b</sup> 9490.6 <sup>c</sup>	6.8 $\pm$ 0.2	1710	32	12641.8	9.8 $\pm$ 0.5	1990	18
[N II] $\lambda$ 6548 <sup>d</sup>		9441.7 $\pm$ 2.9	0.62 $\pm$ 0.09	1160 $\pm$ 150	...	12618 $\pm$ 5	1.4 $\pm$ 0.2	1310 $\pm$ 150	...
H $\alpha$ $\lambda$ 6563 <sup>d</sup>		9460.9 $\pm$ 1.9	4.4 $\pm$ 0.4	1200 $\pm$ 100	...	12636 $\pm$ 3	5.2 $\pm$ 0.5	1300 $\pm$ 150	...
[N II] $\lambda$ 6583 <sup>d</sup>		9492.2 $\pm$ 2.9	1.8 $\pm$ 0.3	1160 $\pm$ 150	...	12686 $\pm$ 5	4.1 $\pm$ 0.4	1310 $\pm$ 150	...
[S II] $\lambda$ 6724	KSPEC	9693.9	1.0 $\pm$ 0.2	1120	6.2	12960.3	1.0 $\pm$ 0.2	850	4.4
[S III] $\lambda$ 9069	KSPEC	13076.9	0.74 $\pm$ 0.08	900	8.7	17467.1	1.1 $\pm$ 0.3	630	3.5
[S III] $\lambda$ 9532	KSPEC	13174.3	2.0 $\pm$ 0.08	930	20	...	...	...	...
He I $\lambda$ 10830	KSPEC	15615.5	2.1 $\pm$ 0.08	1070	27	20873.8	4.8 $\pm$ 0.3	1540	16
[O I] $\lambda$ 6300	CGS4	...	...	...	...	12142.8	< 1.6	(1300)	...
H $\alpha$ + [N II]	CGS4	...	...	...	...	12650.4	7.1 $\pm$ 0.7	1860	10
[S II] $\lambda$ 6724	CGS4	...	...	...	...	12959.6	1.0 $\pm$ 0.3	1130	3.2

<sup>a</sup>Uncorrected for instrumental broadening.

<sup>b</sup>Observed wavelength of H $\alpha$  $\lambda$ 6563.

<sup>c</sup>Observed wavelength of [N II] $\lambda$ 6583.

<sup>d</sup>Emission line values as determined by model fit.

Note. — The parenthetical velocities are adopted values based on the average FWHM of the other, stronger emission lines.

Table 6. CO Emission Line Data

Source	Site	line	$\nu_{v=0}$ (GHz)	$v_{\text{offset}}^a$ (km s <sup>-1</sup> )	$\Delta v_{\text{res}}$ (km s <sup>-1</sup> )	$T_{\text{rms}}^b$ (mK)	$S_{\text{CO}}\Delta v$ (Jy km s <sup>-1</sup> )	$L'_{\text{CO}}^c$ ( $\times 10^9 h^{-2}$ K km s <sup>-1</sup> pc <sup>2</sup> )	$M(\text{H}_2)^d$ ( $\times 10^{10} h^{-2}$ M <sub>⊙</sub> )
IRAS F09105+4108	15m	CO(3 → 2)	239.853	-104	37	1.7	<7.7	<3.0	<1.2
	30m	CO(3 → 2)	239.853	0	31	6.2	<8.2	<3.1	<1.2
				625	30	3.3	<4.3	<1.6	<0.66
	30m	CO(2 → 1)	159.907	0	38	4.6	<6.4	<5.6	<2.2
937				38	3.3	<4.7	<4.1	<1.6	
IRAS F15307+3252	15m	CO(4 → 3)	239.415	-108	38	1.2	<5.6	<4.5	<1.8
	30m	CO(4 → 3)	239.415	0	30	5.7	<7.4	<6.0	<2.4 <sup>e</sup>
				188	30	8.4	<11	<8.9	<3.5
				-188	30	8.4	<11	<8.8	<3.5
				814	30	3.6	<4.7	<3.8	<1.5
			-814	30	3.0	<3.9	<3.1	<1.2	
PG 1634+706	12m	CO(2 → 1)	98.647	0	49	0.46	<3.8	<23	<9.2 <sup>f</sup>
PG 1634+706	15m	CO(5 → 4)	246.584	0	36	1.6	<7.4	<7.1	<2.8

<sup>a</sup>The difference between the velocity the receivers were tuned to and the the systemic velocity of the source.

<sup>b</sup>The rms temperatures are given in terms of main beam brightness temperature.

<sup>c</sup>Assuming  $q_0 = 0.5$ ,  $H_0 = 100 h \text{ km s}^{-1} \text{ Mpc}^{-1}$ .

<sup>d</sup>Assuming  $\alpha = 4 M_{\odot} (\text{K km s}^{-1} \text{ pc}^2)^{-1}$  (see text).

<sup>e</sup>The  $3\sigma$  upper limit of  $M(\text{H}_2)$  reported by Yun, Scoville, & Evans (1998) over the redshift range 0.9240-0.09275 is  $9.8 \times 10^9 h^{-2} M_{\odot}$ .

<sup>f</sup>The  $3\sigma$  upper limit of  $M(\text{H}_2)$  reported by Barvainis et al. (1998) is  $2.0 \times 10^{10} h^{-2} M_{\odot}$ .

Table 7. Observed Emission-Line Ratios

Source	$\frac{[\text{OIII}]\lambda 5007}{\text{H}\alpha}$	$\frac{[\text{OIII}]}{\text{H}\beta}$	$\frac{[\text{NII}]\lambda\lambda 6548+6583}{\text{H}\alpha}$	$\frac{[\text{SII}]\lambda 6724}{\text{H}\alpha}$
HyLIGs				
IRAS F09105+4108	3.9 <sup>a</sup>	...	$0.55 \pm 0.2$	$0.23 \pm 0.11$
IRAS F15307+3252	$3.0 \pm 0.4$	$> 11.1 \pm 0.3$	$1.1 \pm 0.2$	$0.19 \pm 0.10$
<i>IRAS</i> Bright Galaxies				
Seyfert2	$1.8 \pm 1.0$	$10.2 \pm 4.6$	$1.3 \pm 0.7$	$0.41 \pm 0.26$
LINERs	$0.16 \pm 0.10$	$1.7 \pm 1.0$	$1.7 \pm 1.1$	$0.69 \pm 0.41$
H II	$0.10 \pm 0.11$	$0.64 \pm 0.52$	$0.62 \pm 0.24$	$0.27 \pm 0.06$

<sup>a</sup>Determined from  $[\text{O III}] \lambda 5007 / \text{H}\beta = 12$  (Kleinmann et al. 1988) and  $\text{H}\alpha / \text{H}\beta \sim 3.1$ . The  $\text{H}\alpha / \text{H}\beta$  ratio is based on the determination by Kleinmann et al (1988) that  $E(B - V) < 0.15$  for F09105+4108.

## REFERENCES

- Antonucci, R. & Barvainis, R. 1988, *ApJ*, 332, L13
- Barvainis, R. 1996, in *CO: Twenty-five Years of Millimeter-wave Spectroscopy*, eds. W. B. Latter et al. (Dordrecht: Kluwer), 335
- Barvainis, R., Alloin, D., & Antonucci, R. 1989, *ApJ*, 337, L69
- Barvainis, R., Alloin, D., Guilloteau, S., Antonucci, R. 1998, *ApJ*, 492, L13
- Barvainis, R. & Antonucci, R. 1996, *PASP*, 108, 187
- Barvainis, R., Tacconi, L., Antonucci, R., Alloin, D., & Coleman, P. 1994, *Nature*, 371, 586
- Broadhurst, T. & Lehar, J. 1995, *ApJ*, 450, L41
- Brown, R. L., & Vanden Bout, P. A. 1991, *AJ*, 102, 1956
- Brown, R. L., & Vanden Bout, P. A. 1992, *ApJ*, 397, L19
- Chini, R., Kreysa, E., Bierman, P. L. 1989, *A&A*, 219, 87
- Close, L. M., Hall, P. B., Liu, C. T., & Hege, E. K. 1995, *ApJ*, 452, L9
- Cutri, R. M., Huchra, J. P., Low, F. J., Brown, R. L., & Vanden Bout, P. A. 1994, *ApJ*, 424, L65
- Downes, D., Solomon, P. M., & Radford, S. J. E. 1995, *ApJ*, 453, L65
- Downes, D., Solomon, P. M., Sanders, D. B., & Evans, A. S. 1996, *A&A*, 313, 91
- Draine, B. T., & Lee, H. M. 1984, *ApJ*, 285, 89
- Eisenhardt, P. R., Armus, L., Hogg, D. W., Soifer, B. T., Neugebauer, G., Werner, M. W. 1996, *ApJ*, 461, 72



- Elston, R., McCarthy, P. J., Eisenhardt, P., Dickinson, M., Spinrad, H., Januzzi, B. T., & Mahoney, P. 1994, *AJ*, 107, 910
- Evans, A. S., Sanders, D. B., Mazzarella, J. M., Solomon, P. M., Downes, D., Kramer, C., & Radford, S. J. E. 1996, *ApJ*, 457, 658
- Graham, J. R. & Liu, M. C. 1995, *ApJ*, 449, L29
- Guelin, M., Kramer, C., & Wild, W. 1995, *IRAM Newsletter*, 19, 17
- Guilloteau, S. et al. 1997, *A&A*, in press
- Güsten, R., Serabyn, E., Kasemann, C., Schinckel, A., Schneider, G., Schulz, A., & Young, K. 1993, *ApJ*, 402, 537
- Hill, G. J., Thompson, K. L., & Elston, R. 1993, *ApJ*, 414, 1
- Hines, D. C. 1991, *ApJ*, 374, L9
- Hines, D. C. 1994, Ph.D. Thesis, University of Texas
- Hines, D. C., Schmidt, G. D., Smith, P. S., Cutri, R. M., & Low F. J. 1995, *ApJ*, 450, L1
- Hines, D. C. & Wills, B. J. 1993, *ApJ*, 415, 82
- Hodapp, K., Hora, J. L., Irwin, E., & Young, T. 1994, *PASP*, 106, 87
- Hodapp, K., Hora, J. L., Hall, D. N., Cowie, L. L., et al. 1996, *New Astronomy*, 1, 176
- Januzzi, B. T., Elston, R., Schmidt, G. D., Smith, P. S., & Stockman, H. S. 1994, *ApJ*, 429, L49
- Jim, K. T. C. et al. 1997, *PASP*, in preparation
- Kay, L. E. & Miller, J. S. 1989, *BAAS*, 21, 1099

- Kim, D.-C. 1995, Ph.D. Thesis, University of Hawaii
- Kim, D.-C., Sanders, D. B., Veilleux, S., Mazzarella, J. M., & Soifer, B. T. 1995, *ApJS*, 98, 129
- Kleinmann, S. G., Hamilton, D., Keel, W. C., Wynn-Williams, C. G., Eales, S. A., Becklin, E. E., & Kuntz, K. D. 1988, *ApJ*, 328, 161
- Kleinmann, S. G., & Keel, W. C. 1987, in *Star Formation in Galaxies*, ed. Carol J. Lonsdale Persson (NASA C.P. 2466), 559
- Liu, M. C., Graham, J. R., & Wright, G. S. 1996, *ApJ*, 470, 771
- Matthews, H. E. 1992, in *The James Clerk Maxwell Telescope: A Guide for the Prospective User*, ed. H. E. Matthews (Joint Astronomy Center, Hilo)
- Moshir, M., et al. 1992, *Explanatory Supplement to the IRAS Faint Source Catalog, Version 2*, JPL D-10015 8/92 (Pasadena: JPL) (FSC)
- Ohta, K., Yamada, T., Nakanishi, K., Kohno, K., Akiyama, M., & Kawabe, R. 1996, *Nature*, 382, 426
- Omont, A., Petitjean, P., Guilloteau, S., McMahon, R. G., Solomon, P. M., & Pecontal, E. 1996a, *Nature*, 382, 428
- Omont, A., McMahon, R. G., Cox, P., Kreysa, E., Bergeron, J., Pajot, F., & Storrie-Lombardi, L. J. 1996b, *A&A*, 315, 1
- Osterbrock, D. E., Tran, H. D., Veilleux, S. 1992, *ApJ*, 389, 196
- Pozzetti, L., Madau, P., Zamorani, G., Ferguson, H. C., & Bruzual, G. A. 1998, *MNRAS*, in press

- Sanders, D. B. 1991, in *Dynamics of Galaxies and Their Molecular Cloud Distributions*, eds F. Combes and F. Casoli (Dordrecht: Kluwer), 417
- Sanders, D. B. & Mirabel, I. F. 1985, *ApJ*, 298, L31
- Sanders, D. B. & Mirabel, I. F. 1996, *ARA&A*, 34, 749
- Sanders, D. B., Phinney, E. S., Neugebauer, G., Soifer, B. T., & Matthews, K. 1989, *ApJ*, 347, 29
- Sanders, D. B., Scoville, N. Z., & Soifer, B. T. 1988c, *ApJ*, 335, L1
- Sanders, D. B., Scoville, N. Z., & Soifer, B. T. 1991, *ApJ*, 370, 158
- Sanders, D. B., Scoville, N. Z., Tilanus, R. P. J., Wang, Z., & Zhou, S. 1993, in *Back to the Galaxy*, eds S. Holt and F. Verter (New York: AIP), 311
- Sanders, D. B., Soifer, B. T., Elias, J. H., Madore, B. F., Matthews, K., Neugebauer, G., & Scoville, N. Z. 1988a, *ApJ*, 325, 74
- Sanders, D. B., Soifer, B. T., Elias, J. H., Neugebauer, G., & Matthews, K. 1988b, *ApJ*, 328, L35
- Sanders, D. B., Young, J. S., Scoville, N. Z., Soifer, B. T., & Danielson, G. E. 1987, *ApJ*, 312, L5
- Schmidt, M. & Green, R. F. 1983, *ApJ*, 269, 352
- Scoville, N. Z., Padin, S., Sanders, D. B., Soifer, B. T., & Yun, M. S. 1993, *ApJ*, 415, L75
- Scoville, N. Z., & Sanders, D. B. 1987, in *Interstellar Processes*, eds D. Hollenbach and H. Thronson (Dordrecht: Reidel), 21

- Scoville, N. Z., Sanders, D. B., Sargent, A. I., Soifer, B. T., Scott, S. L., & Lo, K. Y. 1986, ApJ, 311, L47
- Scoville, N. Z., Yun, M. S., Windhorst, R. A., Keel, W. C., & Armus, L. 1997, ApJ, 485, L21
- Serjeant, S., Lacy, M., Rawlings, S., King, L. J., & Clements, D. L. 1995, MNRAS, 276, L31
- Soifer, B. T., Cohen, J. G., Armus, L., Matthews, K., Neugebauer, G., & Oke, J. B. 1995, ApJ, 443, L65
- Soifer, B. T., Neugebauer, G., Armus, L., Shupe, D. L. 1996, AJ, 111,649
- Soifer, B. T., Neugebauer, G., Matthews, K., & Armus, L. 1994, ApJ, 433, L69
- Solomon, P. M., Downes, D., & Radford, S. J. E. 1992a, ApJ, 398, L29
- Solomon, P. M., Radford, S. J. E., & Downes, D. 1992b, Nature, 356, 318
- Surace, J.A., Sanders, D.B. Vacca, W.D., Veilleux, S., & Mazzarella, J.M. 1998, ApJ, 492, 116
- Trentham, N. 1995, MNRAS, 277, 616
- Tsuboi, M. & Nakai, N. 1992, PASJ, 44, L241
- Tytler, D. & Fan, X. 1992, ApJS, 79, 1
- Veilleux, S., Kim, D.-C., Sanders, D. B., Mazzarella, J. M., & Soifer, B. T. 1995, ApJS, 98, 171
- Veilleux, S. & Osterbrock, D. E. 1987, ApJS, 63, 295
- Wainscoat, R. J. 1996, University of Hawaii Telescopes at Telescopes at Mauna Kea Observatory - User Manual, University of Hawaii

Wink, J. E., Guilloteau, S., & Wilson, T. L. 1997, *A&A*, 322, 427

Young, J. S., Kenney, J., Lord, S., & Schoerb, F. P. 1984, *ApJ*, 287, L65

Yun, M. S., Scoville, N. Z., & Evans, A. S. 1998, in *Highly Redshifted Radio Lines*, eds. C.

Carilli, S. J. E. Radford, K. Menten, & G. Langston, in press

Figure Captions

Figure 1. Broad-band images of the IRAS F09105+4108; a & b) I-band images with  $56'' \times 56''$  and  $\sim 180'' \times 180''$  fields of view, respectively. c & d) K'-band images with  $56'' \times 56''$  and  $143'' \times 143''$  fields of view, respectively. For all images, North is up and E is to the left.

Figure 2. Broad-band images of the IRAS F15307+3252; a & b) R-band images with  $60'' \times 60''$  and  $\sim 180'' \times 180''$  fields of view, respectively. c & d) K'-band images with  $60'' \times 60''$  and  $180'' \times 180''$  fields of view, respectively. For all images, North is up and E is to the left.

Figure 3. I-band Image of PG 1634+706 with a  $72'' \times 72''$  field of view.

Figure 4. KSPEC spectroscopy of IRAS F09105+4108 covering the observer-frame wavelength range 7000–17500 Å. The pixel sampling for the R, I2, J1, and H-bands are 7.4, 8.5, 12, and 14  $\mu\text{m pixel}^{-1}$ , respectively.

Figure 5. KSPEC spectroscopy of IRAS F15307+3252 covering the observer-frame wavelength range 8600–22400 Å. Note that the feature in panel (a) at 17620 Å is an OH sky line. The pixel sampling for the I2, J2, H, and K'-bands are 8.5, 12, 14, and 20  $\mu\text{m pixel}^{-1}$ , respectively. Panel (e) is a CGS4 spectrum of the H $\alpha$  + [N II] and [S II]  $\lambda$ 6724 lines. The pixel sampling for the CGS4 spectrum is 4.4  $\mu\text{m pixel}^{-1}$ .

Figure 6. KSPEC spectrum of [O III]  $\lambda$ 5007 and H $\alpha$  emission from PG 1634+706. The pixel sampling for the H and K'-bands are 12 and 14  $\mu\text{m pixel}^{-1}$ , respectively. Note that the broad Fe II complex is also evident redward of 12000Å.

Figure 7. JCMT 15m and IRAM 30m spectra of IRAS F09105+4108 ( $z = 0.4417$ ). The intensity scale is main-beam brightness temperature (IRAM) and antenna temperature

corrected for aperture losses (JCMT). A linear baseline has been subtracted from each spectrum. The zero velocity corresponds to the average redshift of optical/near-infrared emission lines observed for IRAS F09105+4108.

Figure 8. JCMT 15m and IRAM 30m spectra of IRAS F15307+3252 ( $z = 0.926$ ). The intensity scale is main beam brightness temperature (IRAM) and antenna temperature corrected for aperture losses (JCMT). A linear baseline has been subtracted from each spectrum. The zero velocity corresponds to the average redshift of optical/near-infrared emission lines observed for IRAS F15307+3252.

Figure 9. NRAO 12m and JCMT 15m spectra of PG 1634+706 ( $z = 1.338$ ). The intensity scale is main beam brightness temperature (NRAO) and antenna temperature corrected for aperture losses (JCMT). A linear baseline has been subtracted from each spectrum. The zero velocity corresponds to the systemic velocity of the QSO as determined by Tytler & Fan (1992) averaged with the redshift of the [O III]  $\lambda 5007$  and  $H\alpha$  emission lines.

Figure 10. Four emission-line diagnostic diagram plots of IRAS F09105+4108 and IRAS F15307+3252. The [O I]  $\lambda 6300$  /  $H\alpha$  ratio for F09105+4108 has been determined from the data in Kleinmann et al. (1988), where the  $H\alpha$  flux was determined from the  $H\beta$  flux and the observation that the extinction in F09105+4108 is negligible. Additional data of H II regions, LINERS, and Seyfert are taken from data compiled by Osterbrock et al. (1992).

Figure 11. (a).  $L'_{CO}$  vs.  $L_{ir}$  plot of *IRAS* galaxies and QSOs. Arrows denote upper limits. References for CO and infrared (ir) data: LIGs - Sanders, Scoville, & Soifer (1991); ULIGs - Sanders (1991); IRAS F09105+4108 - This work (CO) and Kleinmann et al. (1988) (ir); IRAS F15307+3252 - This work (CO) and Cutri et al (1994) (ir); IZw 1 - Barvainis, Alloin, & Antonucci (1989); Mrk 1014 - Sanders, Scoville, & Soifer (1988a); 3C 48 - Scoville et al. (1993); PG 1634+706 - This work (CO) and Sanders et al. (1989) (ir). (b).  $L_{ir}/L'_{CO}$  vs.  $L_{ir}$

plot of the same sources. Arrows denote upper limits.

Figure 12. Rest-frame SEDs of IRAS F09105+4108, IRAS F15307+3252, and PG 1634+706.

The dashed lines represent smooth fits to the data. References for data: For IRAS F09105+4108 - all data are from Kleinmann et al. 1988. For IRAS F15307+3252 - all data are from Cutri et al. 1994. For PG 1634+706 - all data from Sanders et al. (1989), except for the  $560 \mu\text{m}$  data (Chini, Kreysa, & Bierman 1989) and data between  $10^3$ – $10^5 \mu\text{m}$  (Antonucci & Barvainis 1988).



This figure "asefig1.jpg" is available in "jpg" format from:

<http://arxiv.org/ps/astro-ph/9806091v1>

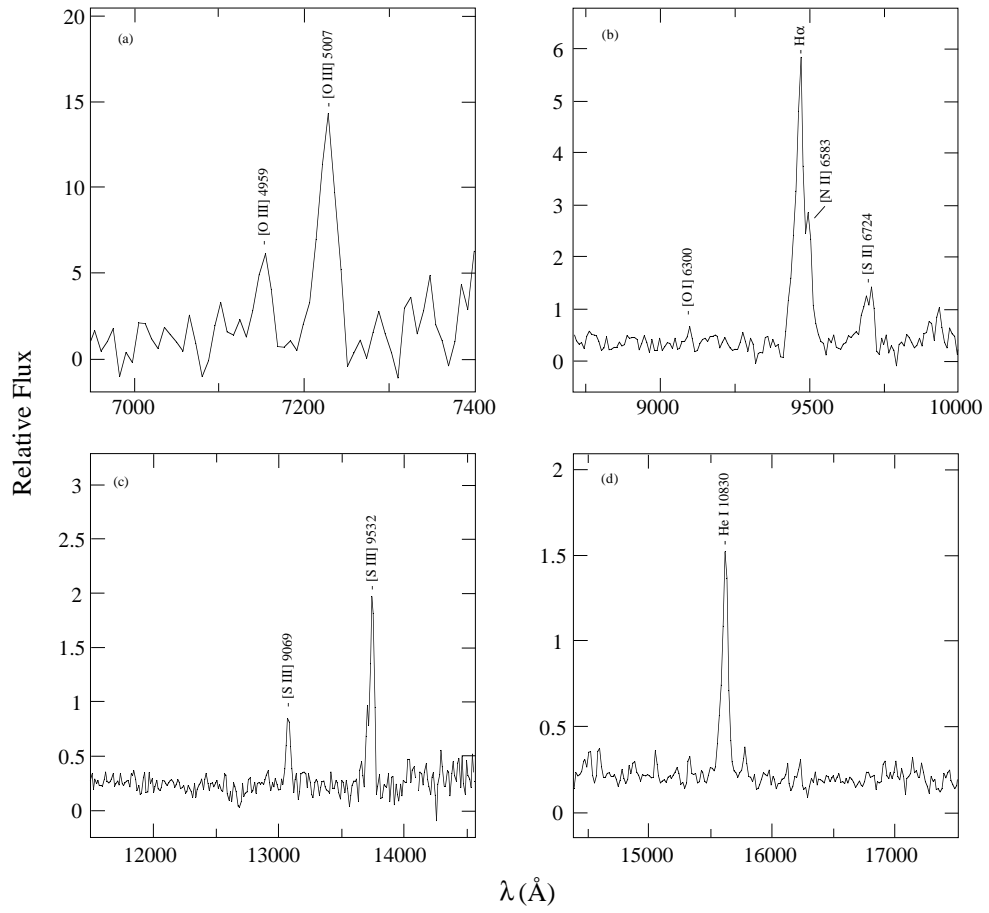
This figure "asefig2.jpg" is available in "jpg" format from:

<http://arxiv.org/ps/astro-ph/9806091v1>

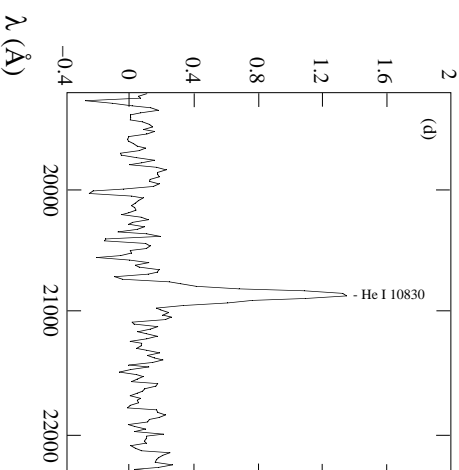
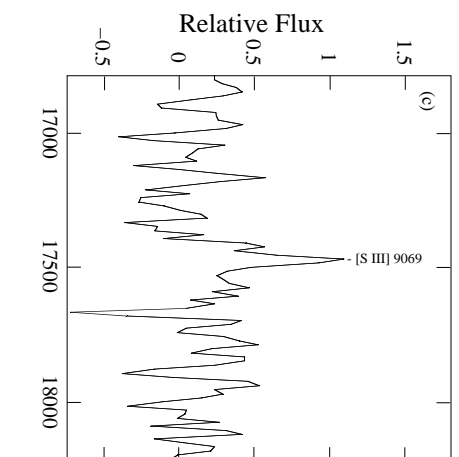
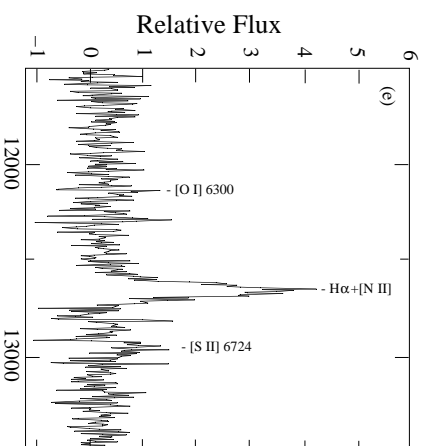
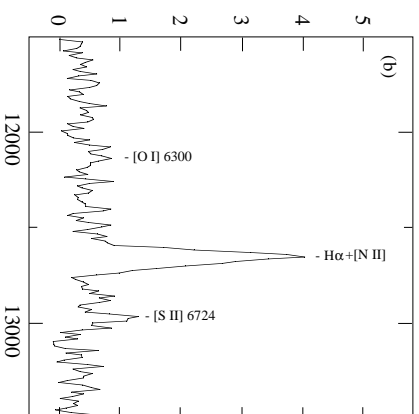
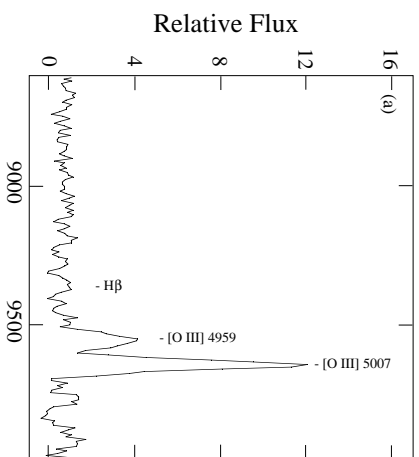
This figure "asefig3.jpg" is available in "jpg" format from:

<http://arxiv.org/ps/astro-ph/9806091v1>

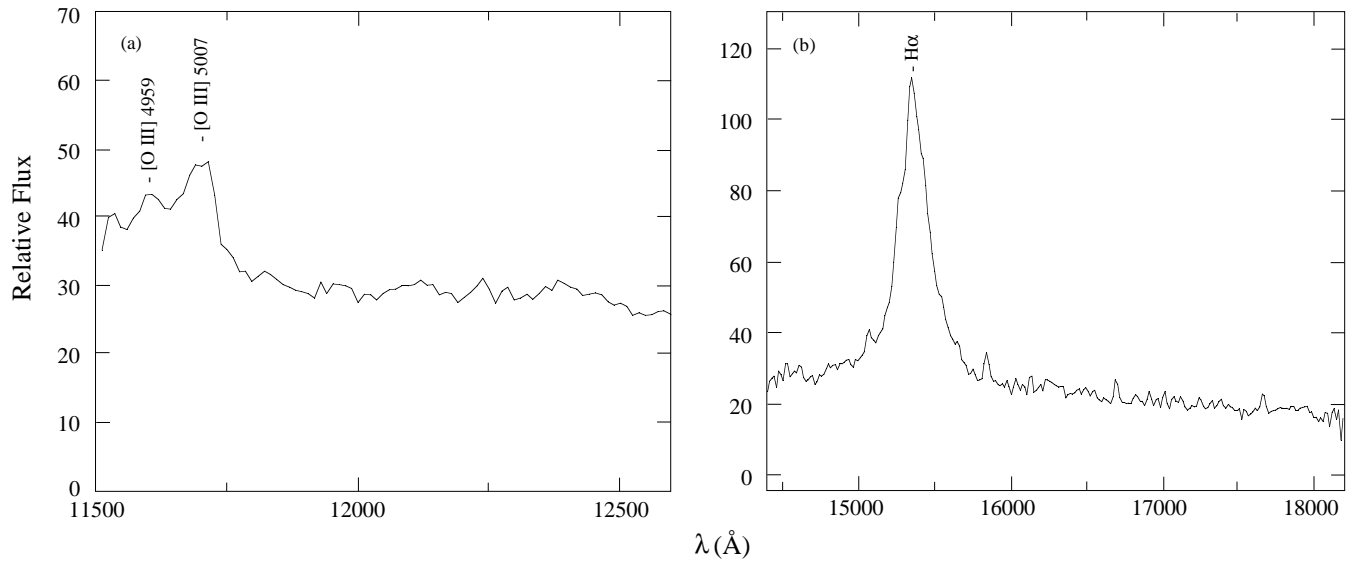
IRAS F09105 + 4108



IRAS F15307 + 3252

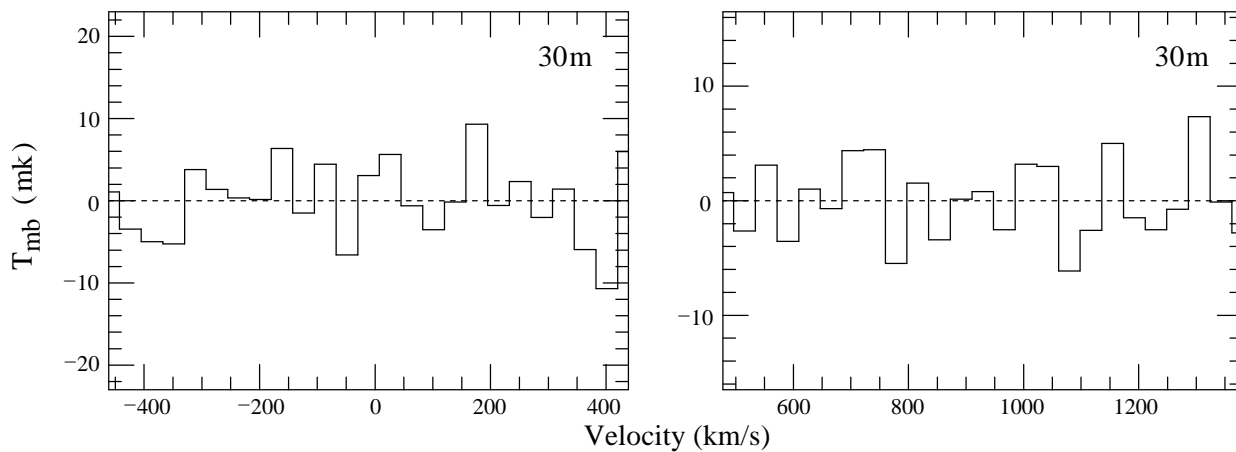


PG 1634+706

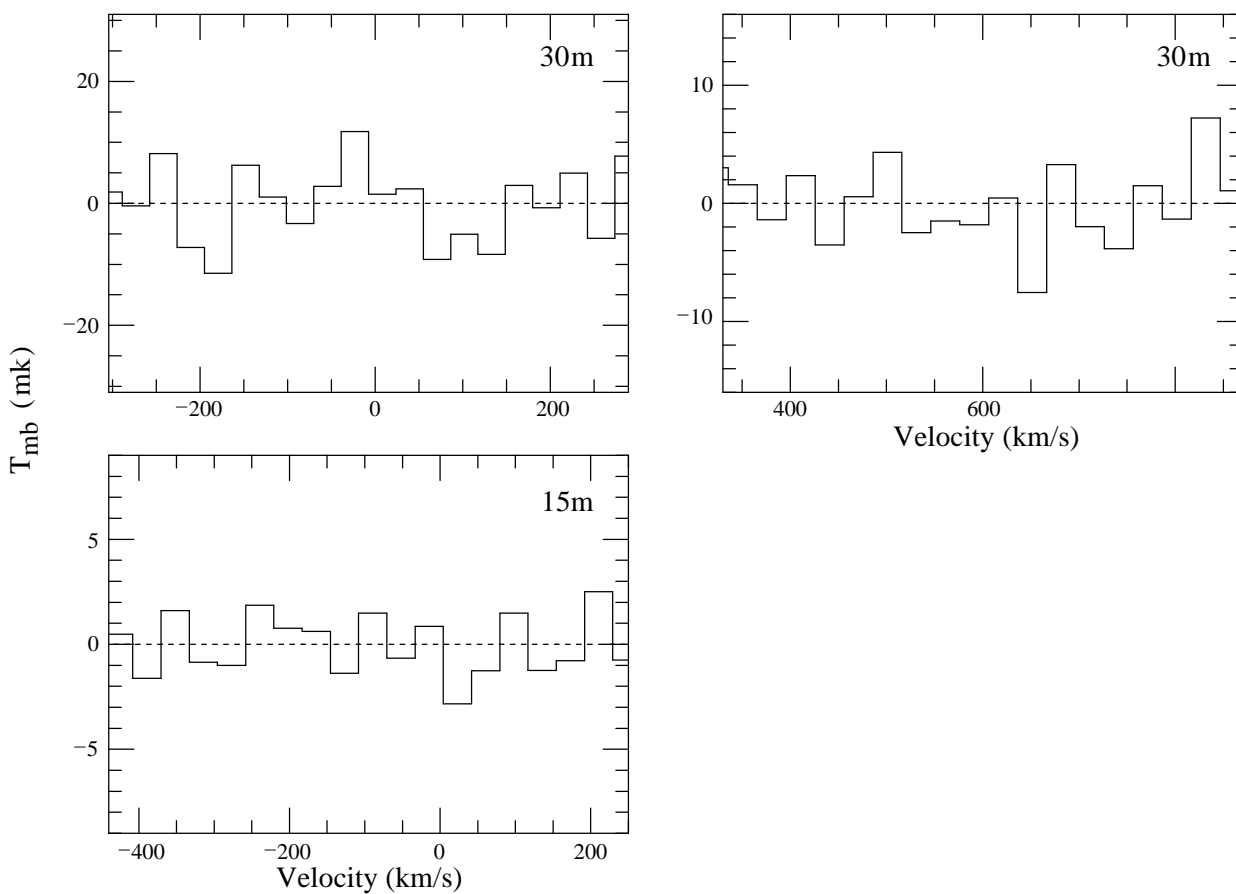


IRAS F09105 + 4108 ( $z=0.4417$ )

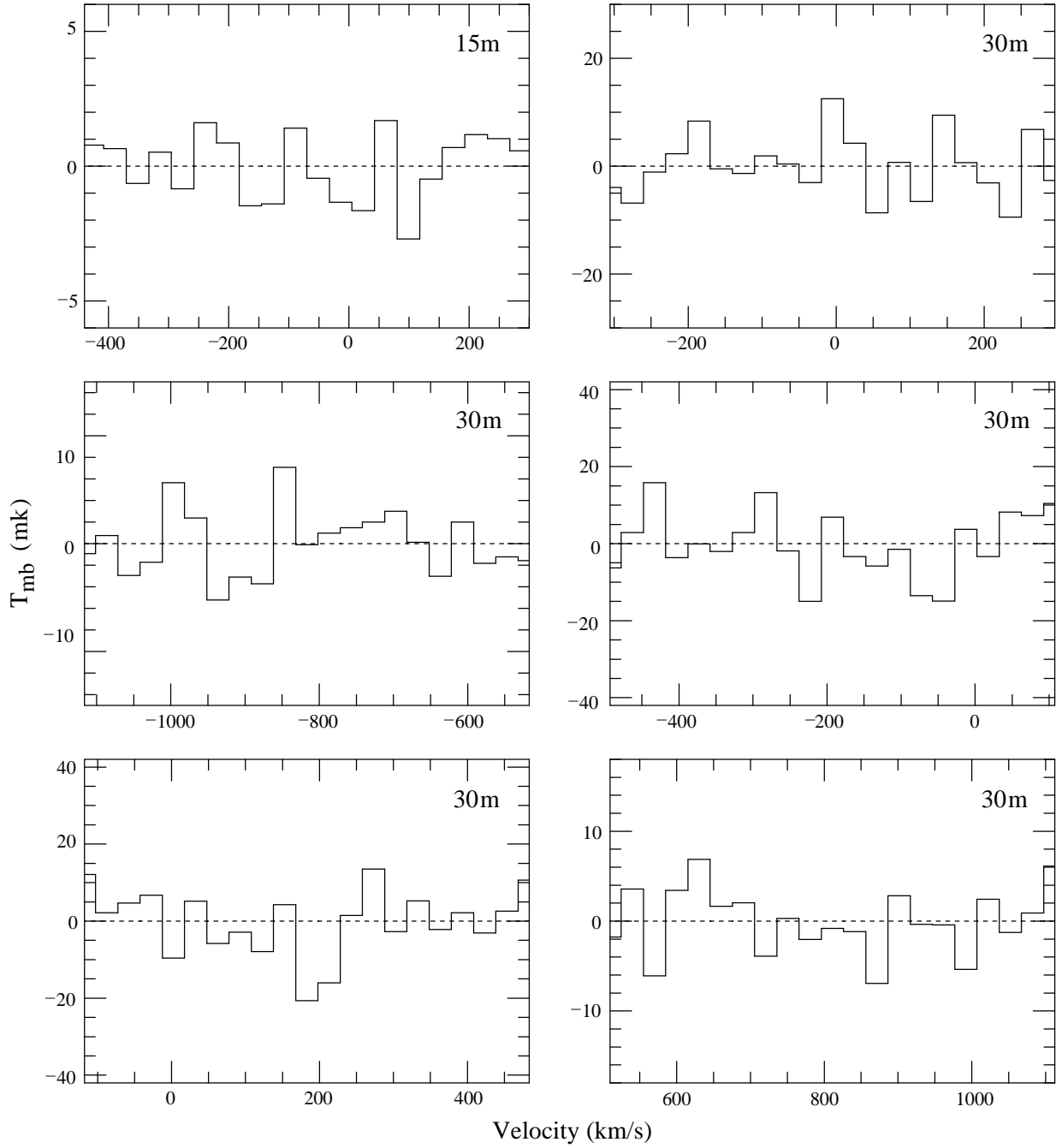
CO (2-1)



CO (3-2)

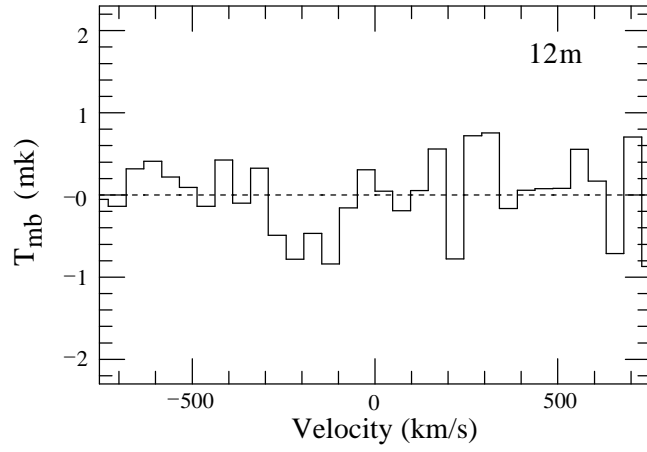


IRAS F15307 + 3252 ( $z=0.926$ )  
CO (4-3)





PG 1634+706 ( $z=1.337$ )  
CO (2-1)



CO (5-4)

